

DOI: 10.1002/((please add manuscript number))

Article type: Communication

Aggregation induced multi-length scaled morphology enabling 11.76% efficiency in all-polymer solar cells using printing fabrication

Lei Zhu, Wenkai Zhong, Chaoqun Qiu, Bosai Lyu, Zichun Zhou, Ming Zhang, Jingnan Song, Jinqiu Xu, Jing Wang, Jazib Ali, Wei Feng, Zhiwen Shi, Xiaodan Gu, Lei Ying, Yongmin Zhang and Feng Liu*

Dr. Lei Zhu, Chaoqun Qiu, Zichun Zhou, Prof. Dr. Yongmin Zhang, Prof. Dr. Feng Liu

Department of Polymer Science and Engineering, School of Chemistry and Chemical Engineering, Shanghai Jiao Tong University, Shanghai 200240, P. R. China

E-mail: fengliu82@sjtu.edu.cn

Bosai Lyu, Ming Zhang, Jingnan Song, Jinqiu Xu, Jing Wang, Jazib Ali, Prof. Dr. Zhiwen Shi, Prof. Dr. Feng Liu

School of Physics and Astronomy, and Collaborative Innovation Center of IFSA (CICIFSA), Shanghai Jiao Tong University, Shanghai 200240, P. R. China

Dr. Lei Zhu, Wenkai Zhong, Prof. Dr. Lei Ying

State Key Laboratory of Luminescent Materials and Devices, South China University of Technology, Guangzhou 510640, P. R. China

Prof. Dr. Xiaodan Gu

School of Polymer Science and Engineering, The University of Southern Mississippi, Hattiesburg, MS 39406, USA

Dr. Wei Feng

This is the author manuscript accepted for publication and has undergone full peer review but has not been through the copyediting, typesetting, pagination and proofreading process, which may lead to differences between this version and the [Version of Record](#). Please cite this article as doi: [10.1002/adma.201902899](https://doi.org/10.1002/adma.201902899).

This article is protected by copyright. All rights reserved.

State Key Laboratory of Fluorinated Materials, Zibo City, Shandong Province 256401, P. R. China

Keywords: organic photovoltaics, multi-length scaled morphology, thin film printing, in situ characterization, x-ray scattering

Abstract: All-polymer solar cells (all-PSCs) exhibit excellent stability and readily tunable ink viscosity, especially suitable for printing preparation of large-scale devices. At present, the efficiency of state-of-the-art all-PSCs fabricated by spin-coating method has exceeded 11%, laying the foundation for the preparation and practical utilization of printed devices. In this study, a high power conversion efficiency (PCE) of 11.76% is achieved based on PTzBI-Si:N2200 all-PSCs processing with 2-Methyltetrahydrofuran (MTHF, an environmentally friendly solvent) and preparation of active layers by slot die printing, which is the top efficient for all-PSCs. Conversely, the PCE of device processed by high-boiling point chlorobenzene (CB) is less than 2%. Through the study of film formation kinetics, volatile solvents can freeze the morphology in a short time, and a more rigid conformation with strong intermolecular interaction combined with the solubility limit of PTzBI-Si and N2200 in MTHF, resulting in the formation of fibril network in bulk-heterojunction (BHJ). The multi-length scaled morphology ensures fast transfer of carriers and facilitates exciton separation, which boost carrier mobility and current density, thus improve the device performance. These results are of great significance for large-scale printing fabrication of high-efficiency all-PSCs in the future.

All-polymer solar cell (all-PSC) that uses p-/n- polymer mixture to construct bulk heterojunction nanostructure to harvest solar radiation is quite different from small molecular acceptor and polymer blends in terms of material crystallization and phase separation.^[1-6] Polymer mixtures of different properties naturally intent to phase separate to form large sized phase separation if a large interaction parameter presented, resulting in inefficient charge separation and collection.^[7-9] However, recent progresses show quite steep climbing of power conversion efficiency (PCE) for all-PSCs, reaching a value over 10%,^[10-12] under systematic optimization, leaving a large gap to be filled in understanding the mechanism of morphology evolution. Polymer blends that reach nano-scaled

This article is protected by copyright. All rights reserved.

phase separation in organic photovoltaic application have distinctive advantages. They are more suitable for printing fabrication because of their good film forming ability and mechanical flexibility, prominent device stability, and readily tunable ink viscosity.^[13-17] Such benefits make all-PSC unique in scalable OPV fabrication, which also leads to boosted interest in understanding and manipulating the morphology. Initiative efforts on all-PSC printing have been surveyed, showing PCEs way below device made by spin-coating.^[16, 18] The mystery lies in morphology control, of which BHJ thin film is typical non-equilibrium nature that film drying kinetics dictates the final nanostructure composed of crystalline networks and mixed and phase separated domains.^[19-21] It has been shown that solar cells using polymer:NFA blends processed by slot die printing has exceed 11% in PCE,^[22-28] from which we think that fine-tuning of morphology in all-PSCs could reach a similar level once a proper kinetic pathway can be locked. The crystallization of conjugated polymers usually takes the fibril texture that guides carrier transport efficiently.^[29-32] In the scenario of all-PSC, the mixing region is the key. Conjugated polymer crystallization can hardly reach equilibrium, and the main chain conformational disorder results in chain segments incorporation into crystalline registration,^[33] protruding other chain segments out and participated in mixing region. Thus it is an interesting system to investigate the optoelectronic process of BHJ morphology and device performance correlation under complicated morphology. We use poly{[N,N-9-bis(2-octyldodecyl)-naphthalene-1,4,5,8-bis-(dicarboximide)-2,6-diyl]-alt-5,50-(2,20-bithiophene)} (N2200) as the n-type acceptor polymer and poly{[(4,8-bis(5-(2-ethylhexyl)thiophen-2-yl)benzo[1,2-b:4,5-b']dithiophene-co-4,8-di(thien-2-yl)-2-(1,1,1,3,5,5-heptamethyltrisiloxan-3-yl)hexyl]-6-octyl[1,2,3]triazolo[4,5-f]isoindole-5,7(2H,6H)-dione} (PTzBI-Si) as the p-type donor polymer, and use printing fabrication to make BHJ layers of all-PSCs with different solvents to tune the starting solution aggregation status and the film drying

This article is protected by copyright. All rights reserved.

kinetics. Average PCE that exceeds of 11.25% (11.76% maximum) is achieved for the first time in all-PSC. Soft and hard x-ray scattering techniques as well as microscopy methods are used to investigate the morphology details,^[34, 35] from which we see that interaction parameter between polymers and solvents, the intermolecular interaction, solubility and material crystallization are critical parameters that influence the final morphology and device performance of printed solar cells.^[36]

The chemical structure and absorption of PTzBI-Si and N2200 are shown in **Figure 1a-b**. Chlorobenzene (CB) and 2-Methyltetrahydrofuran (MTHF) were used as the solvents due to their difference in solubility and boiling temperature. Hansen solubility parameters were first calculated by group contribution methods^[37] to estimate the polymer-solvent interaction: $\delta_{\text{CB}}=19.58$, $\delta_{\text{MTHF}}=18.14$, $\delta_{\text{PTzBI-Si}}=18.48$, $\delta_{\text{N2200}}=18.95$. Such results suggest that PTzBI-Si in MTHF has better solubility while N2200 dissolve better in CB. The solubility of PTzBI-Si and N2200 in CB and MTHF was measured and summarized in **Table S1**, which matched well with the trend of solubility parameters. Polymer in different solution could show quite different chain conformation, resulting in different structural and optical properties. However, the absorption of PTzBI-Si in MTHF is red-shifted by 43 nm compared to that in CB. N2200 in MTHF showed a more pronounced long wavelength shoulder peak at 800 nm in MTHF. Thus PTzBI-Si and N2200 in MTHF adopt a more rigid conformation with stronger pi-pi stacking, which is different from Hansen parameter prediction, due to the complicated backbone/side-chain structure of conjugated polymer. Such feature could physically crosslink the polymer in MTHF solution, and viscous organogels will be formed in when setting still for several hours at room temperature^[38]. In addition, MTHF has a boiling point (80 °C) much lower than that of CB (132 °C), which vaporizes much quicker in printing fabrication that quickly vitrify the film to suppress large scaled aggregations.

This article is protected by copyright. All rights reserved.

Solar cells were fabricated using a configuration of glass/ITO/PEDOT:PSS/PTzBI-Si:N2200/C60-N/Ag and an effective area of 0.04 cm^2 was defined by a shadow mask. C60-N was used as the electronic transport layer because it can reduce the effective work function of electrode and enable the use of more stable metals.^[39] The photovoltaic parameters are shown in **Figure 1c-d** and **Table 1**. The as printed devices using MTHF solvent showed a PCE of 9.57% with a V_{OC} of 0.89V, a J_{SC} of 15.41 mA cm^{-2} , and a fill factor (FF) of 69.82%. Thermal annealing (TA) at 130 °C for 10 min improved PCE to 10.35 % (an average PCE of 9.96% from over 50 devices) with a V_{OC} of 0.88 V, a J_{SC} of 16.19 mA cm^{-2} and an FF of 72.65%. In addition to TA, solvent vapor annealing (SVA) is subsequently used, leading to a PCE of 11.76% with a V_{OC} of 0.88 V, a J_{SC} of 17.62 mA cm^{-2} and an FF of 75.78%. Such value is the highest in printed all-PSCs, which is even higher than optimized spin-coated devices. Moreover, large-area (1.00 cm^2) PSCs were fabricated using slot die printing and the best performed device offers a PCE of 10.15% with a V_{OC} of 0.87 V, a J_{SC} of 16.08 mA cm^{-2} and an FF of 72.66%, which showed its potential of printing fabrication (J - V curve was shown in **Figure S1**). On the contrary, devices prepared using CB solvent were much lower in performances, showing PCEs around 1-2% under different fabrication conditions (**Table 1** for details). The maximum external quantum efficiency (EQE) values of devices with the best processing conditions of CB and MTHF are 24.81% and 79.41%, yielding integrated current of 4.58 and 17.62 mA cm^{-2} , in good agreement with J - V measurements. **Figure S2a** showed the light intensity dependence of J_{SC} follows the power law correlation $J_{SC} \propto (P_{light})^\alpha$,^[40] where P_{light} is the illumination intensity and α is the exponential factor. The α values are 0.934 and 0.983 for optimized CB (TA+SVA) and MTHF (TA+SVA) devices, respectively, suggesting a much weaker bimolecular recombination in MTHF printed devices. The light intensity and V_{OC} correlation was also executed. A slope of $2 kT/q$ (thermal voltage at 300 K) in

the plot of V_{OC} versus the natural logarithm of the light intensity indicates that the recombination is of monomolecular or trap-assisted nature, while a slope of kT/q states the recombination mechanism is bimolecular type. As shown in **Figure S2b**, slopes of 1.614 and 1.199 kT/q were obtained from CB (TA+SVA) and MTHF (TA+SVA) printed devices, thus bimolecular recombination dominates in MTHF processed devices. The carrier mobility of devices were measured by applying the space-charge limited current (SCLC) method using electron only (ITO/ZnO/PTzBI-Si:N2200/Al) and hole only (ITO/PEDOT:PSS/PTzBI-Si:N2200/MoO_x/Al) devices,^[41] and the corresponding curves and mobilities are shown in **Figure S3** and summarized in **Table 1**. The hole and electron mobilities of devices processed by MTHF are two orders of magnitude higher than that in CB processed devices. Carrier mobility increased after TA and SVA. Devices processed by optimized MTHF condition exhibit the highest carrier mobility (μ_e : $3.07 \times 10^{-4} \text{ cm}^2 \text{ V}^{-1} \text{ s}^{-1}$, μ_h : $2.25 \times 10^{-3} \text{ cm}^2 \text{ V}^{-1} \text{ s}^{-1}$). The improved mobility leads to monomolecular recombination as we have seen previously in amorphous BHJ mixtures.^[42] Such high value in good carrier transporting balance gives rise to improved FF and J_{SC} , leading high PCEs. Moreover, we also studied the stability of printed all-polymer solar cell device (solvent: MTHF, TA+SVA) under nitrogen atmosphere. The device was stored in glove box at 20 °C and measured the efficiency at intervals of 24 hours. As shown in **Figure S4**, the device showed 96.8% of the initial PCE retained after 20 days. Moreover, the PCE retained over 98% of the original value after 96 hours annealing at 80 °C in glovebox, which exhibits excellent device stability.

We then investigated the morphology details of all-polymer BHJ thin films to explore the structure-property relationship. As shown in **Figure 2**, the atomic force microscopy (AFM) height and phase images, fibril texture was seen from MTHF processed thin films with diameters around 35 nm, while CB processed thin film showed large sized aggregations induced by crystallites agglomeration.

Infrared spectroscopy technique was coupled to AFM (scanning near-field optical microscopy (SNOM)) to identify chemical content in phase image.^[43, 44] As seen in **Figure S5**, N2200 has a distinctive absorption at 1308 cm^{-1} in FTIR, which can be used to highlight N2200 in BHJ thin films. As seen in **Figure 2**, dark fibrils of tens of nanometer size were seen, which were assigned to N2200. Different processing condition led to different fibril size and density. For thin films processed from CB, dark aggregations were seen, which was from N2200 crystallites agglomeration. BHJ thin film morphology was further checked by transmission electron microscopy (TEM). CB processed thin films showed aggregations similar to that seen in AFM. MTHF processed thin film showed micrometer long fibrils that intertwined into a network with a mesh size of $\sim 100\text{ nm}$. There were also tiny fibrils that were blurred due to the high contrast from N2200 fibrils. Thermal annealing and solvent annealing led to increased fibril diameter, due to improved material crystallization.

Resonant soft x-ray scattering (R-SoXS) was used to investigate the phase separation size statistics using photon energy that gave best contrast. As seen in **Figure S6**, CB processed films showed uncompleted peak that blocked by beam stop, thus large phase separation above 400 nm was recorded. Such value is in good agreement with TEM and AFM characterization. Such a large phase separation retards exciton splitting and collection, thus poor J_{SC} and FF were seen. MTHF processed films showed the peak location at $q = 0.049, 0.057$ and 0.060 nm^{-1} corresponding to the center-to-center distance of $127.6, 110.7$ and 104.6 nm under the condition of as cast, TA and TA+SVA preparation condition. These dimensions corresponded to the average distance between fibrils in the blend films. The R-SoXS intensity showed continuous growth for as-cast, TA and TA+SVA processed thin films, thus the extent of phase separation improved under the preparation sequence. In addition, we also investigated the morphology of spin-coated thin films (**Figure S7**). While CB

processing still gave rise to N2200 aggregations, MTHF processing yielded a much smoother thin film, which is due to the quick drying kinetics that suppressed the long fibril growth for N2200.

The crystalline order of conjugated polymer constitutes an important sector in BHJ thin film morphology that plays a critical role in carrier transport. The crystalline structure of neat and blend films was studied by grazing incidence x-ray diffraction (GIXD). The 2D diffraction patterns and 1D line-cuts were summarized in **Figure S8** and **Figure 3**. Both donor and acceptor polymers were of good crystalline order as seen from neat film GIXD. For PTzBI-Si, a (100) diffraction peak at 0.25 \AA^{-1} with a *d*-spacing of 25.22 \AA in the in-plane (IP) direction and a (010) diffraction peak at 1.69 \AA^{-1} with a *d*-spacing of 3.72 \AA in the out-of-plane (OOP) were recorded in both of CB and MTHF processed films. Similarly, the neat N2200 films exhibited a side chain stacking (100) packing at 0.25 \AA^{-1} with a *d*-spacing of 25.22 \AA , a main chain stacking (001) at 0.46 \AA^{-1} with a *d*-spacing of 13.62 \AA in the IP direction, and a pi-pi stacking (010) peak at 1.58 \AA^{-1} with a *d*-spacing of 3.97 \AA in the OOP direction. Quite sharper (001) peak was seen for CB processed N2200 film. Thus the main chain persistence length is longer, which could lead to strong pi-pi stacking and aggregation. BHJ thin film crystalline order and feature analysis were shown in **Figure 3b-d** and in **Figure S9**. The overlapping of (100) and (010) peak position made it hard to analysis specific polymer packing, and the peak summation analysis was used to evaluate the BHJ structure order as a whole. The crystal packing for both polymers in neat and blended thin films took a face-on orientation, as seen from 2D diffraction profiles. The peak intensity, crystal coherence length (CCL) for both (100) and (010) packing plane showed continuous increase following as-cast, TA, TA+SVA processing sequence for both CB and MTHF processed thin films. In $0.4\text{--}0.5 \text{ \AA}^{-1}$ region that containing PTzBI-Si (200) and N2200 (001) peak also showed consecutive growth under the processing sequence, and a two gaussian peak

This article is protected by copyright. All rights reserved.

summation could been seen. Thus both polymers showed crystallinity improvement. CB as-cast thin film showed much stronger (100) peak intensity and larger CCL comparing to MTHF as-cast thin film, while (010) peak showed the opposite trend. Thus CB is more efficient in inducing side chain stacking and MTHF is more efficient in improving pi-pi stacking. Such feature can be traced back from the chemical structure origin and solubility parameter difference. CB as an aromatic solvent could help to solubilize backbone, making polymer chain in a extended geometry, which, during drying process, the alkyl-to-alkyl self-assembly thermodynamics could more easily to surpass the entropy penalty to order. MTHF is more facial in interaction with alkyl side chains, giving more favorable Hansen solubility parameters (the side chain mass is similar to backbone mass for both conjugated polymer), the backbone was kept in close contact geometry, and during drying the side-chain assembly is retarded due to backbone restrains. The device parameter and phase separation versus processing condition were plotted in **Figure 3d** and **Figure S9b**. Quite good correlations can be seen from device performances and structure details in MHTF processed blends. The improved crystallinity, especially in (010) direction could lead to improved carrier transport, thus giving rise to elevated FF. The reduced length scale of phase separation give rise to enlarged specific inner surface area (inverse scaling to length scale of phase separation) affording improved J_{SC} . Device parameters develop in the same trend in thin film crystallization, indicating that the framework in such BHJ blends is of crystalline nature. Such morphology gives quite high carrier mobility and bimolecular recombination becomes the major carrier-decaying channel since bimolecular recombination could be reduced at mixing region or donor-acceptor interfaces due to efficient charge splitting and carrier transport.

The film drying kinetics and morphology evolution of the blend films were investigated by using in situ GIXD and grazing incidence small angle scattering (GISAXS) with results shown in **Figure S10-**

11. ^[45] **Figure 4a** showed the real-time evolution of fitted GIXD peak height, distance and CCL in IP (100) and OOP (010) direction. In CB processing, the wet film dried slowly and (100)/(010) peak show up after 5.1s. Those peaks grew rapidly during 5.1 to 11.7 s in crystal size and peak intensity accordantly, and then got saturated. Correlation length by analyzing GISAXS profiles (Debye-Bucherer method) yielded a size jumping in the same time period, and the size scale is quite small (~24 nm) that can only be assigned to small sized phase separation in BHJ thin film. MTHF processed thin film showed a different drying kinetics. No well-established crystalline packing can be observed before 2.7s, and then suddenly within a second, material crystallization got saturated and stabilized in both (100) and (010) packing. Correlation length profile developed in consistency with crystalline peak intensity profile. The quick crystallization occurred during the near end of solvent evaporation, as seen from the solvent evaporation traces, which agrees with previous report.^[45] There were small aggregates or crystallites appeared before the sharp-dropping in solvent trace, as seen from in situ GIXD and GISAXS analytical results. The longer sedimentation of these species in CB solution affords longer time that they can agglomerate, leading to large sized aggregations. The quick drying in MTHF processing freeze the thin film kinetically, which can only induce long N2200 fibrils as seen in previous characterization, leading to improved morphology and device performances. The pre-aggregation to long fibril network formation scheme was illustrated in **Figure 4b**, showing detailed mechanism.

The above-discussed results revealed the important structure-property relationship in all-PSCs. Achieving high efficiency all polymer BHJ solar cells needs to better balance phase separation and polymer mixing to suppress large scaled phase separation. Such consideration is critical, if not more important than light-absorption and energy level tuning, in material and solvent selection. The

success of the current PTzBI-Si:N2200 using MTHF casting is a classic demonstration. The high crystallinity nature of N2200 made it difficult to compatible with many donor polymers since large sized aggregation is a taboo in OPV. PTBzBI-Si is an interesting polymer with moderate crystallinity, and more importantly, it could mix well with N2200 in blending zone. We see in interaction parameter measurement^[46] that a quite small chi value (~0.02) in-between PTBzBI-Si and N2200 (**Figure S12**), which could form homogeneous mixture in the mixing region and also suppressing large scaled phase separation. In term of solvent selection, we try to use Hansen parameter to gauge the solvent-molecule interaction. However, the complicated chain structure makes this effort hardly useful. While solubility is certainly an important factor that needs to be taken into account, we start to focus on solvent boiling point. In printing fabrication, solvent vaporize much slower comparing to spin-coating, which could lead to large sized aggregations, as seen in our CB case. Quick vaporization in a manageable time scale could quickly freeze the thin film to induce homogeneity. We have also shown that the crystallization of conjugated polymers speeds up quite quickly in the near-drying state (solid to solvent ratio close to 1:1), during which the solubility limit quickly sediments solutes to form crystallites. If a fibril network could be established in this time frame, a good BHJ morphology could thus be obtained. Such consideration shifts our attention to the solution state or early drying state. We see in characterization that both PTzBI-Si and N2200 could form weak aggregates (indicated by absorption profiles in MTHF solution), not yet to a 3D chain registration state. Such feature in a conjugated polymer case would be resulted from inter-chain pi-pi stacking, forming localized nanostructures that fully swelled by solvent. Such scenario is quite similar to physical crosslinking, and if we set aside the solution for a longer time, organogel can be seen (**Figure S13**). In printing, the chain aggregated species could be translated into final morphology, via

material diffusion and crystallization and to form long fibrils as we see in the current case. Such fibrils cannot be standing-alone, as judged by the fibril diameter and length. There should be many chains only participated through chain segments, leaving other sides to cooperate in mixing region or in other polymer fibrils, forming a hierarchical structure that helps to collect carriers more effectively.^[47] Since both PTzBI-Si and N2200 were seen to be crystalline, thus p type and n type polymers could form crystalline fibrils to boost electron and hole transport. In this picture, the mixing region of all polymer blends is of advantage, since interchain transport is much more efficient than intrachain hopping,^[48] and the spilted carriers can be efficiently collected though these chains to the fibril highways and then get collected. Such advantage originates from the non-equilibrium crystallization of conjugated polymers, making all-polymer unique in OPV sub-categories. Thermal and solvent vapor annealing slightly induces crystalline order of both materials to achieve a better transporting network. Thus quite high FF and low bimolecular recombination can be obtained. Such a nanostructure that containing p type and n type crystalline fibril network, with “flagella” incorporated in the mixing region, is an interesting new multi-length scaled morphology that help to boosting the PCE in all polymer solar cells.

To conclude, 11.76% high efficiency all-polymer solar cells have been achieved by using PTzBI-Si as donor and N2200 as acceptor under printing device fabrication. The success of this demonstration lies in the detailed morphology optimization, which uses a volatile solvent to freeze the mixing morphology at an earlier state of phase separation and maintaining a moderate crystalline fibril network. Subsequent thermal and solvent vapor annealing better optimizes the morphology by elevating thin film crystallinity to improve carrier transport and reduce recombination. Quite good structure-property relationship has been established, which show that a multi-length scaled

morphology can be useful in improve the PCE of solar cells. Such morphology, obtained by manipulating material miscibility, crystallization, and film drying kinetics, deserves attention in future OPV research.

Supporting Information

Supporting Information is available from the Wiley Online Library or from the author.

Acknowledgements

This work was financially supported by the grant from the National Natural Science Foundation of China (No. 21734009, 11327902, 11574204, 11774224 and 21822505). Portions of this research were carried out at beam line 7.3.3 and 11.0.1.2 at the Advanced Light Source, Molecular Foundry, Lawrence Berkeley National Laboratory, which was supported by the DOE, Office of Science, and Office of Basic Energy Sciences.

Received: ((will be filled in by the editorial staff))

Revised: ((will be filled in by the editorial staff))

Published online: ((will be filled in by the editorial staff))

This article is protected by copyright. All rights reserved.

References

- [1] B. Fan, L. Ying, Z. Wang, B. He, X.-F. Jiang, F. Huang, Y. Cao, *Energy Environ. Sci.* **2017**, *10*, 1243.
- [2] S. Li, H. Zhang, W. Zhao, L. Ye, H. Yao, B. Yang, S. Zhang, J. Hou, *Adv. Energy Mater.* **2016**, *6*, 1501991.
- [3] Z. Li, W. Zhang, X. Xu, Z. Genene, D. Di Carlo Rasi, W. Mammo, A. Yartsev, M. R. Andersson, R. A. J. Janssen, E. Wang, *Adv. Energy Mater.* **2017**, *7*, 1602722.
- [4] Y. Wang, Z. Yan, H. Guo, M. A. Uddin, S. Ling, X. Zhou, H. Su, J. Dai, H. Y. Woo, X. Guo, *Angew. Chem., Int. Ed.* **2017**, *56*, 15304.
- [5] L. Gao, Z.-G. Zhang, L. Xue, J. Min, J. Zhang, Z. Wei, Y. Li, *Adv. Mater.* **2016**, *28*, 1884.
- [6] Z. Li, X. Xu, W. Zhang, X. Meng, Z. Genene, W. Ma, W. Mammo, A. Yartsev, M. R. Andersson, R. A. J. Janssen, E. Wang, *Energy Environ. Sci.* **2017**, *10*, 2212.
- [7] C. R. McNeill, B. Watts, L. Thomsen, W. J. Belcher, A. L. D. Kilcoyne, N. C. Greenham, P. C. Dastoor, *Small* **2006**, *2*, 1432.
- [8] C. R. McNeill, N. C. Greenham, *Adv. Mater.* **2009**, *21*, 3840.
- [9] C. R. McNeill, H. Ade, *J. Mater. Chem. C* **2013**, *1*, 187.
- [10] Z. Li, L. Ying, P. Zhu, W. Zhong, N. Li, F. Liu, F. Huang, Y. Cao, *Energy Environ. Sci.* **2019**, *12*, 157.

This article is protected by copyright. All rights reserved.

- [11] H. Yao, F. Bai, H. Hu, L. Arunagiri, J. Zhang, Y. Chen, H. Yu, S. Chen, T. Liu, J. Y. L. Lai, Y. Zou, H. Ade, H. Yan, *ACS Energy Lett.* **2019**, *4*, 417.

- [12] B. Fan, L. Ying, P. Zhu, F. Pan, F. Liu, J. Chen, F. Huang, Y. Cao, *Adv. Mater.* **2017**, *29*, 1703906.

- [13] E. Garnier, R. Hajlaoui, A. Yassar, P. Srivastava, *Science* **1994**, *265*, 1684.

- [14] H. Yan, Z. Chen, Y. Zheng, C. Newman, J. R. Quinn, F. Dötz, M. Kastler, A. Facchetti, *Nature* **2009**, *457*, 679.

- [15] Y. Diao, Y. Zhou, T. Kurosawa, L. Shaw, C. Wang, S. Park, Y. Guo, J. A. Reinspach, K. Gu, X. Gu, B. C. K. Tee, C. Pang, H. Yan, D. Zhao, M. F. Toney, S. C. B. Mannsfeld, Z. Bao, *Nat. Commun.* **2015**, *6*, 7955.

- [16] L. Ye, Y. Xiong, S. Li, M. Ghasemi, N. Balar, J. Turner, A. Gadisa, J. Hou, B. T. O'Connor, H. Ade, *Adv. Funct. Mater.* **2017**, *27*, 1702016.

- [17] Y. Liu, T. T. Larsen-Olsen, X. Zhao, B. Andreasen, R. R. Søndergaard, M. Helgesen, K. Norrman, M. Jørgensen, F. C. Krebs, X. Zhan, *Sol. Energy Mater. Sol. Cells* **2013**, *112*, 157.

- [18] X. Gu, Y. Zhou, K. Gu, T. Kurosawa, Y. Guo, Y. Li, H. Lin, B. C. Schroeder, H. Yan, F. Molina-Lopez, C. J. Tassone, C. Wang, S. C. B. Mannsfeld, H. Yan, D. Zhao, M. F. Toney, Z. Bao, *Adv. Energy Mater.* **2017**, *7*, 1602742.

- [19] C. R. McNeill, *Energy Environ. Sci.* **2012**, *5*, 5653.

- [20] M. Schubert, D. Dolfen, J. Frisch, S. Roland, R. Steyrleuthner, B. Stiller, Z. Chen, U. Scherf, N. Koch, A. Facchetti, D. Neher, *Adv. Energy Mater.* **2012**, *2*, 369.

This article is protected by copyright. All rights reserved.

- [21] N. Zhou, H. Lin, S. J. Lou, X. Yu, P. Guo, E. F. Manley, S. Loser, P. Hartnett, H. Huang, M. R. Wasielewski, L. X. Chen, R. P. H. Chang, A. Facchetti, T. J. Marks, *Adv. Energy Mater.* **2014**, *4*, 1300785.
- [22] H. Bin, L. Gao, Z.-G. Zhang, Y. Yang, Y. Zhang, C. Zhang, S. Chen, L. Xue, C. Yang, M. Xiao, Y. Li, *Nat. Commun.* **2016**, *7*, 13651.
- [23] Y. Yang, Z.-G. Zhang, H. Bin, S. Chen, L. Gao, L. Xue, C. Yang, Y. Li, *J. Am. Chem. Soc.* **2016**, *138*, 15011.
- [24] W. Zhao, S. Li, H. Yao, S. Zhang, Y. Zhang, B. Yang, J. Hou, *J. Am. Chem. Soc.* **2017**, *139*, 7148.
- [25] L. Meng, Y. Zhang, X. Wan, C. Li, X. Zhang, Y. Wang, X. Ke, Z. Xiao, L. Ding, R. Xia, H.-L. Yip, Y. Cao, Y. Chen, *Science* **2018**, *361*, 1094.
- [26] J. Hou, O. Inganäs, R. H. Friend, F. Gao, *Nat. Mater.* **2018**, *17*, 119.
- [27] P. Cheng, G. Li, X. Zhan, Y. Yang, *Nat. Photonics* **2018**, *12*, 131.
- [28] C. Yan, S. Barlow, Z. Wang, H. Yan, A. K. Y. Jen, S. R. Marder, X. Zhan, *Nat. Rev. Mater.* **2018**, *3*, 18003.
- [29] T. Liu, L. Huo, S. Chandrabose, K. Chen, G. Han, F. Qi, X. Meng, D. Xie, W. Ma, Y. Yi, J. M. Hodgkiss, F. Liu, J. Wang, C. Yang, Y. Sun, *Adv. Mater.* **2018**, *30*, 1707353.
- [30] H. Fu, Z. Wang, Y. Sun, *Angew. Chem., Int. Ed.*, DOI: 10.1002/anie.201806291.
- [31] Y. Xie, F. Yang, Y. Li, M. A. Uddin, P. Bi, B. Fan, Y. Cai, X. Hao, H. Y. Woo, W. Li, F. Liu, Y. Sun, *Adv. Mater.* **2018**, *30*, 1803045.

This article is protected by copyright. All rights reserved.

- [32] H. Fu, C. Li, P. Bi, X. Hao, F. Liu, Y. Li, Z. Wang, Y. Sun, *Adv. Funct. Mater.* **2019**, *29*, 1807006.
- [33] G. Reiter, J.U. Sommer, *Polymer Crystallization: Observations, Concepts and Interpretations*, Springer, Mulhouse Cedex, CNRS-UHA, France **2003**.
- [34] F. Liu, M. A. Brady, C. Wang, *Eur. Polym. J.* **2016**, *81*, 555.
- [35] J. Song, M. Zhang, M. Yuan, Y. Qian, Y. Sun, F. Liu, *Small Methods* **2018**, *2*, 1700229.
- [36] F. Liu, Y. Gu, X. Shen, S. Ferdous, H.-W. Wang, T. P. Russell, *Prog. Polym. Sci.* **2013**, *38*, 1990.
- [37] C. M. Hansen, *Hansen Solubility Parameters: A User's Handbook, Second Edition*, CRC Press, Boca Raton, FL, **2007**.
- [38] M. Suzuki, K. Hanabusa, *Chem. Soc. Rev.* **2010**, *39*, 455.
- [39] Z. A. Page, Y. Liu, V. V. Duzhko, T. P. Russell, T. Emrick, *Science* **2014**, *346*, 441.
- [40] P. Schilinsky, C. Waldauf, C. J. Brabec, *Appl. Phys. Lett.* **2002**, *81*, 3885.
- [41] A. Carbone, B. K. Kotowska, D. Kotowski, *Phys. Rev. Lett.* **2005**, *95*, 236601.
- [42] B. Xiao, M. Zhang, J. Yan, G. Luo, K. Gao, J. Liu, Q. You, H.-B. Wang, C. Gao, B. Zhao, X. Zhao, H. Wu, F. Liu, *Nano Energy* **2017**, *39*, 478.
- [43] Z. Fei, A. S. Rodin, G. O. Andreev, W. Bao, A. S. McLeod, M. Wagner, L. M. Zhang, Z. Zhao, M. Thiemens, G. Dominguez, M. M. Fogler, A. H. C. Neto, C. N. Lau, F. Keilmann, D. N. Basov, *Nature* **2012**, *487*, 82.

This article is protected by copyright. All rights reserved.

- [44] J. Chen, M. Badioli, P. Alonso-González, S. Thongrattanasiri, F. Huth, J. Osmond, M. Spasenović, A. Centeno, A. Pesquera, P. Godignon, A. Zurutuza Elorza, N. Camara, F. J. G. de Abajo, R. Hillenbrand, F. H. L. Koppens, *Nature* **2012**, *487*, 77.
- [45] F. Liu, S. Ferdous, E. Schaible, A. Hexemer, M. Church, X. Ding, C. Wang, T. P. Russell, *Adv. Mater.* **2015**, *27*, 886.
- [46] J. A. Emerson, D. T. W. Toolan, J. R. Howse, E. M. Furst, T. H. Epps, *Macromolecules* **2013**, *46*, 6533.
- [47] Z. Zhou, S. Xu, J. Song, Y. Jin, Q. Yue, Y. Qian, F. Liu, F. Zhang, X. Zhu, *Nat. Energy* **2018**, *3*, 952.
- [48] R. Noriega, J. Rivnay, K. Vandewal, F. P. V. Koch, N. Stingelin, P. Smith, M. F. Toney, A. Salleo, *Nat. Mater.* **2013**, *12*, 1038.

Author Manuscript

This article is protected by copyright. All rights reserved.

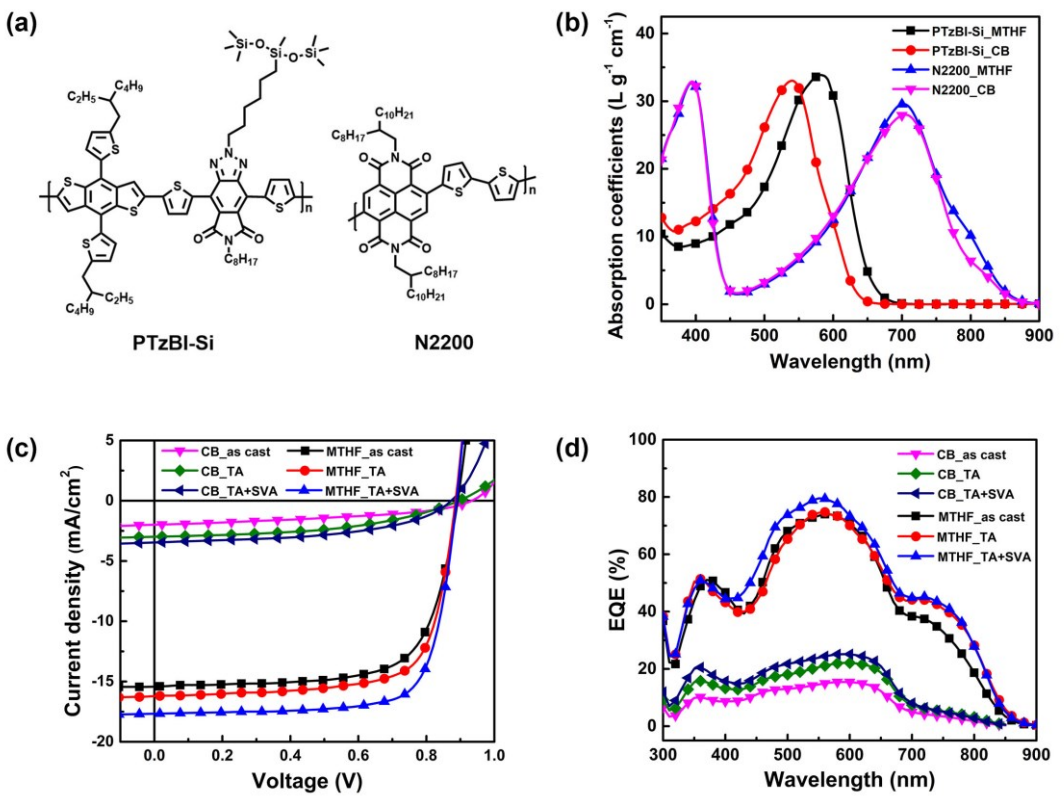


Figure 1. (a) The chemical structures of PTzBI-Si and N2200. (b) UV-vis absorption spectra of PTzBI-Si and N2200 in CB and MTHF at 25 °C (c) J - V curves of PTzBI-Si and N2200 based devices processed with different solvents and post processing methods. (d) EQE curves with integrated current densities.

Author Manuscript

This article is protected by copyright. All rights reserved.

WILEY-VCH

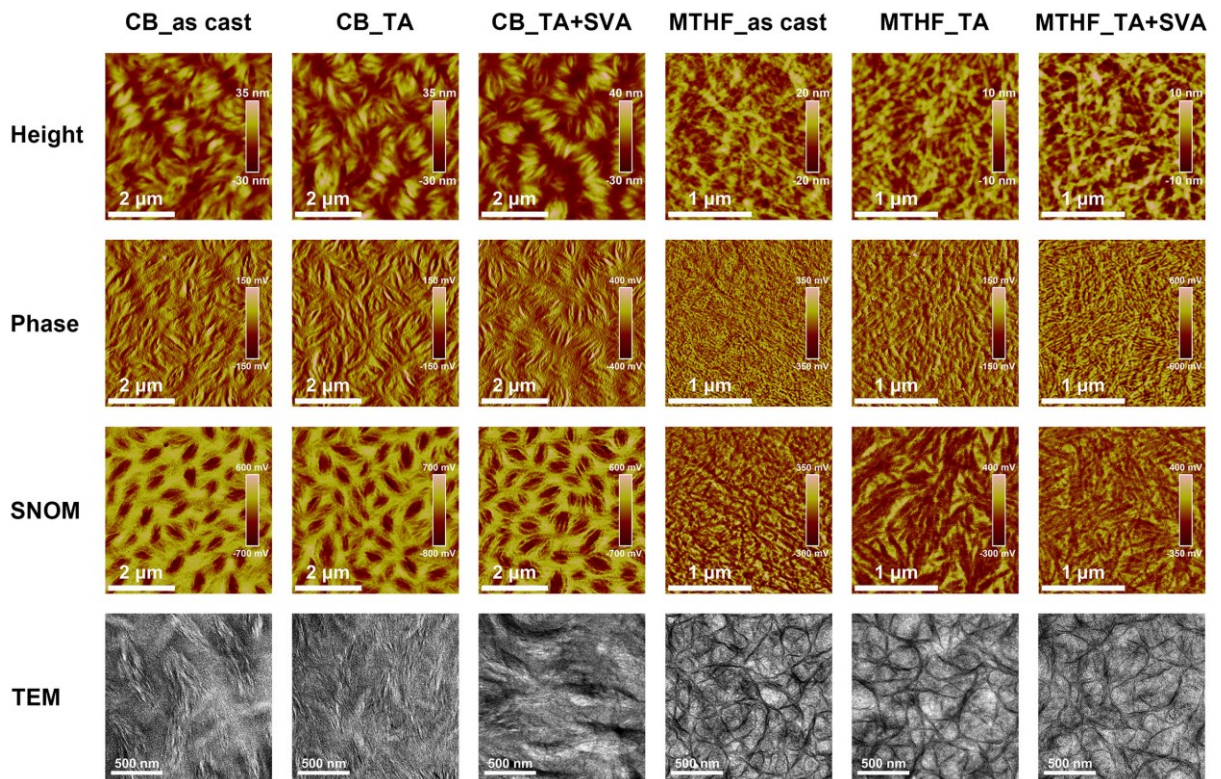


Figure 2. The AFM height (first row), phase (second row), SNOM (third row) and TEM image (fourth row) of PTzBI-SI:N2200 blends processed by slot die printing under different processing condition.

Author Manuscript

This article is protected by copyright. All rights reserved.

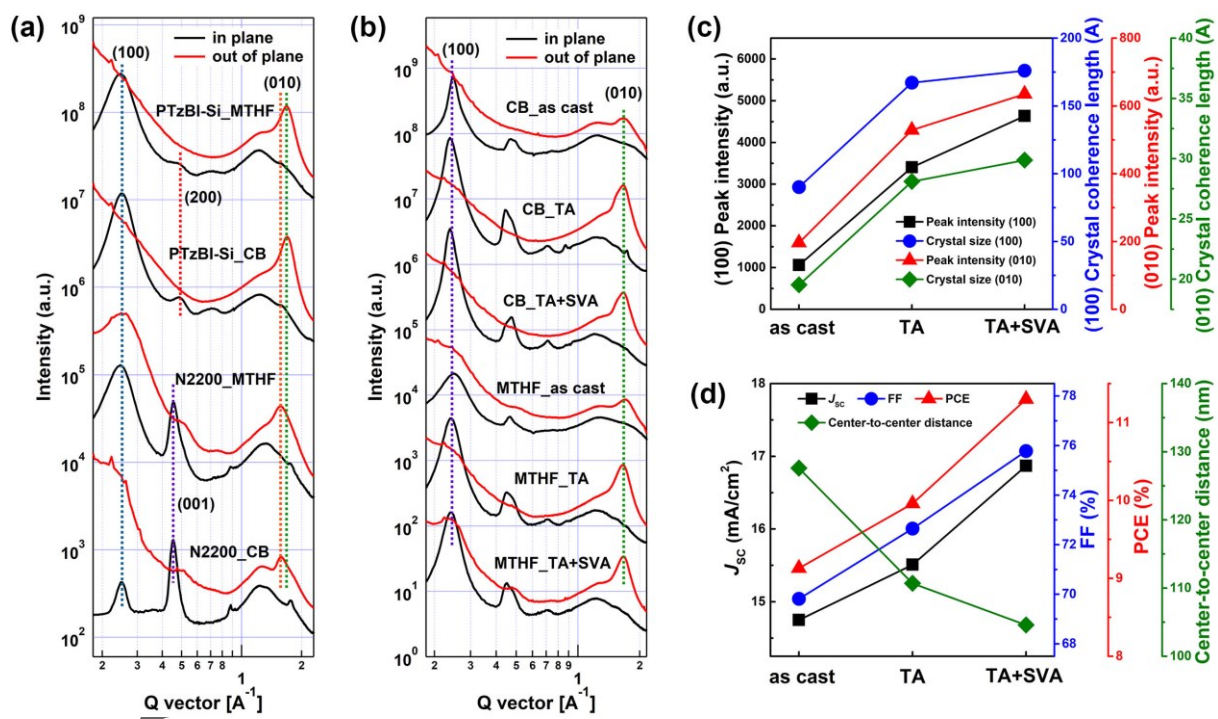


Figure 3. (a) Scattering profiles for pure films of PTzBI-Si and N2200 and (b) blend films under different conditions. (c) The peak height and crystal coherence length of (100) and (010) under different processing solvent or post-treatment. (d) Device parameters and phase separation versus processing condition.

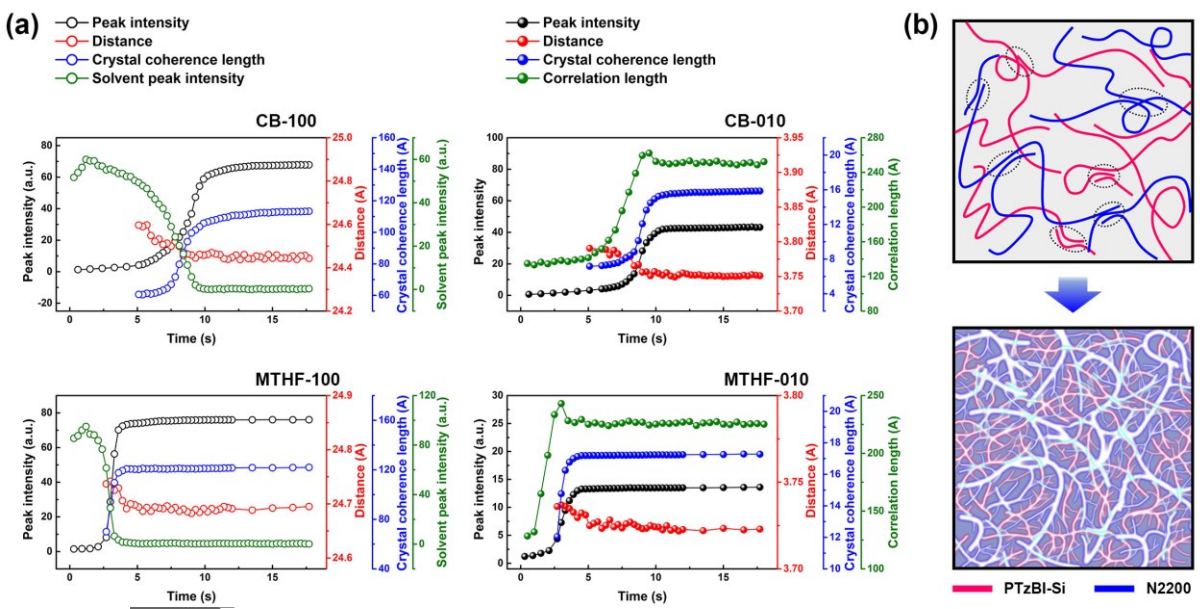


Figure 4. (a) Analysis of in situ GIXD results. Peak fitting of (100) and (010) was used to estimate the peak intensity, distance, crystal coherence length, solvent peak intensity and the correlation length (obtained by Debye-Beuche fitting). (b) Schematic presentation of the morphology-forming process. The polymers aggregate in MTHF solution (top) and fibril network structure formed after solvent removal.

Author Manuscript

This article is protected by copyright. All rights reserved.

Table 1. Photovoltaic parameters of PTzBI-Si and N2200 based devices.

Conditions	Device area [cm ²]	V _{OC} [V]	J _{SC} [mA cm ⁻²]	FF [%]	PCE _{avg} [%]	PCE _{max} [%]	J _{SC} ^{cal} [mA cm ⁻²]	μ _e ^{c)} [cm ² V ⁻¹ s ⁻¹]	μ _h ^{c)} [cm ² V ⁻¹ s ⁻¹]
CB-as print	0.04	0.93	2.76	42.56	1.01 ^{a)}	1.09	2.73	1.68×10^{-6}	2.28×10^{-6}
CB-TA	0.04	0.89	3.98	48.12	1.57 ^{a)}	1.71	3.97	3.77×10^{-6}	6.31×10^{-6}
CB-TA+SVA	0.04	0.87	4.58	51.14	1.83 ^{a)}	2.04	4.50	7.39×10^{-6}	2.02×10^{-5}
MTHF-as print	0.04	0.89	15.41	69.82	9.01 ^{a)}	9.57	14.87	1.01×10^{-4}	6.61×10^{-4}
MTHF-TA	0.04	0.88	16.19	72.65	9.96 ^{a)}	10.35	15.65	1.26×10^{-4}	1.48×10^{-3}
MTHF-TA+SVA	0.04	0.88	17.62	75.78	11.25 ^{a)}	11.76	16.94	3.07×10^{-4}	2.25×10^{-3}
MTHF-TA+SVA	1.00	0.87	16.08	72.65	9.48 ^{b)}	10.15	15.88	-	-

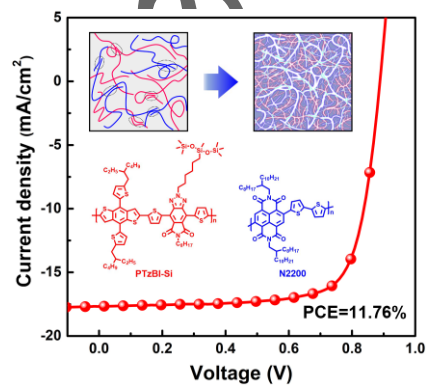
^{a)} average values are obtained from 50 devices;^{b)} average values are obtained from 20 devices;^{c)} average values are obtained from 10 devices

A high power conversion efficiency of 11.76% is achieved by printing fabrication based on PTzBI-Si:N2200 processing with 2-Methyltetrahydrofuran, which is the top efficient for all-PSCs. The multi-length scaled morphology is found in bulk-heterojunction, which ensures fast transfer of carriers and facilitates exciton separation, and boost carrier mobility and current density, thus improve the device performance.

Keywords: organic photovoltaics, multi-length scaled morphology, thin film printing, in situ characterization, x-ray scattering

*Lei Zhu, Wenkai Zhong, Chaoqun Qiu, Bosai Lyu, Zichun Zhou, Ming Zhang, Jingnan Song, Jinqiu Xu, Jing Wang, Jazib Ali, Wei Feng, Zhiwen Shi, Xiaodan Gu, Lei Ying, Yongmin Zhang and Feng Liu**

Aggregation induced multi-length scaled morphology enabling 11.76% efficiency in all-polymer solar cells using printing fabrication



This article is protected by copyright. All rights reserved.